frontiers | Frontiers in Physics

TYPE Original Research
PUBLISHED 04 April 2024
DOI 10.3389/fphy.2024.1366488

OPEN ACCESS

EDITED BY
Yuanyuan Huang,
Chengdu University of Information Technology, China

REVIEWED BY
Shuangqiang Liu,
Sun Yat-sen University, China
Jie Li,
Tianjin University, China

*CORRESPONDENCE
Jian Shen,
shenjian@hainanu.edu.cn

†These authors have contributed equally to this work

RECEIVED 06 January 2024
ACCEPTED 18 March 2024
PUBLISHED 04 April 2024

CITATION
Zeng Y, Zhang P, Li Z, Shen J and Li C (2024), Fabry-perot interferometers with resin scaffolders for high sensitivity temperature sensing.
Front. Phys. 12:1366488.
doi: 10.3389/fphy.2024.1366488

Fabry-perot interferometers with resin scaffolders for high sensitivity temperature sensing

Yu Zeng[1,2†], Pengyu Zhang[1,2†], Zhiqi Li[1,2], Jian Shen[1,2*] and Chaoyang Li[1,2]

[1]School of Information and Communication Engineering, Hainan University, Haikou, China, [2]State Key Laboratory of Marine Resource Utilization in South China Sea, Hainan University, Haikou, China

This study explores the development of an innovative Fabry-Perot Interferometer (FPI) designed for temperature sensing and environmental monitoring. The device is constructed by embedding optical fibers within a 3D-printed resin scaffold, forming a structure with an open Fabry-Perot cavity. Intended as an integral component of Cyber-Physical-Social Systems (CPSS), this FPI structure aims to enhance the system's capacity to sense changes in external environmental conditions. Within the CPSS context, the FPI offers several advantages, including simple manufacturing processes, low production costs, and high sensitivity. These benefits contribute to providing precise environmental feedback to the system, which is essential in implementing effective security and privacy protection strategies. Experimental evaluations have shown that the FPI exhibits a high linear sensitivity of 14.330 nm/°C within a temperature range of 34.9°C–38.5°C, confirming its potential for application in CPSS for temperature monitoring and environmental sensing.

KEYWORDS

3D print, resin scaffold, open fabry-perot resonator, sensor, environmental monitoring

1 Introduction

Recently, Fabry-Perot temperature sensors attracts more and more attention due to the advantage of small size, high sensitivity, electromagnetic interference resistance, and corrosion resistance [1–7]. In many fields such as medical care, environmental monitoring, and food safety [8], It is very sensitive to changes in temperature, so improving the sensitivity of temperature sensors has always been a concern. As with the Fabry-Perot interferometer (FPI) [9–11], various types of fiber optic temperature sensors have been proposed and demonstrated, such as Mach-Zehnder interferometers [12], distributed sensors [13], fiber Bragg grating, and so on [14–16]. Among them, the FPI has attracted widespread attention due to its advantages of low manufacturing difficulty, low cost, and simple structure.

For a typical FPI sensor, its structure consists mainly of two reflective surfaces, when a beam of light is reflected by the two reflective surfaces multiple times, multiple beams of different phases will be generated, and the light of different phases will interfere after entering the optical fiber. In general, the temperature change of the external environment will cause the phase change of the interference light for two reasons: the thermos-optical coefficient (TOC) and the coefficient of thermal expansion (TEC). This is the principle of FPI sensor temperature sensing. Due to the small TOC and TEC of silica, the sensitivity of traditional all-fiber structure sensors is limited. So high TOC or high TEC materials can be combined with FPI sensing structures to improve temperature sensitivity [17].

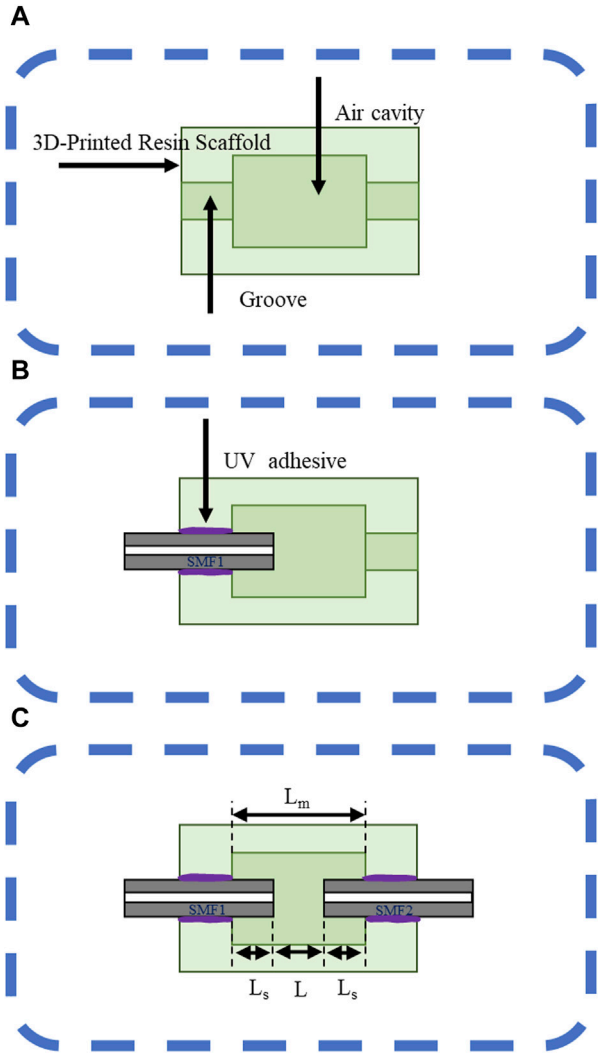

FIGURE 1
Schematic diagram of device fabrication. **(A)** Fabrication of the resin scaffold. **(B, C)** The process of mounting and fixing optical fibers.

In recent years, a method has been proposed to use heat-sensitive materials as auxiliary materials to improve the temperature sensitivity of FPI sensors. B. Sun et al. proposed a novel polymer cap FPI with a temperature response of 249 pm/°C [18]. The sensor is inexpensive to manufacture and the process is very simple, but the polymer cap interference cavity is directly exposed to the air, resulting in insufficient structural strength and easy contamination by the external environment to affect the performance of the sensor. To solve this problem, the polymer was filled into the FPI [10, 19, 20]. In 2018, M.Q. Chen et al. filled the FPI with polydimethylsiloxane (PDMS), which achieved a temperature sensitivity of 2.7035 nm/°C [21]. D. Fu et al. [22] and C. Lang et al. [23] proposed that PDMS and dimethicone oil were injected into the FPI in segments to form a multi-segment air cavity structure. In 2022, H.T. Gao et al., filled a capillary with UV glue, and its temperature sensitivity reached 1226.64 pm/°C [24], but the filling process was complex, and it was difficult to manufacture a thick cavity, even if it had a high TEC, it could not respond to small temperature changes, and the sensitivity was greatly limited. In addition, many materials were combined with FPI sensing structures, such as polymethyl methacrylate (PMMA) [25], Resin [26], Nafion [27], etc.

In this article, we introduce a high-sensitivity temperature sensor designed for intelligent environmental monitoring within Cyber-Physical-Social Systems (CPSS). The sensor's effectiveness has been validated empirically. Engineered to deliver precise temperature readings, our sensor comprises a 3D-printed resin scaffold that embeds dual single-mode optical fibers (SMFs). This configuration facilitates seamless integration with CPSS physical layers. Utilizing a FPI structure, the sensor demonstrated exceptional temperature sensitivity, achieving 14.330 nm/°C, and maintained a linearity of 99.9% across a temperature range from 34.9°C to 38.5°C during testing. Such performance is particularly advantageous in CPSS applications that necessitate stringent temperature regulation and surveillance. Furthermore, attributes such as the sensor's heightened sensitivity, manufacturability, and

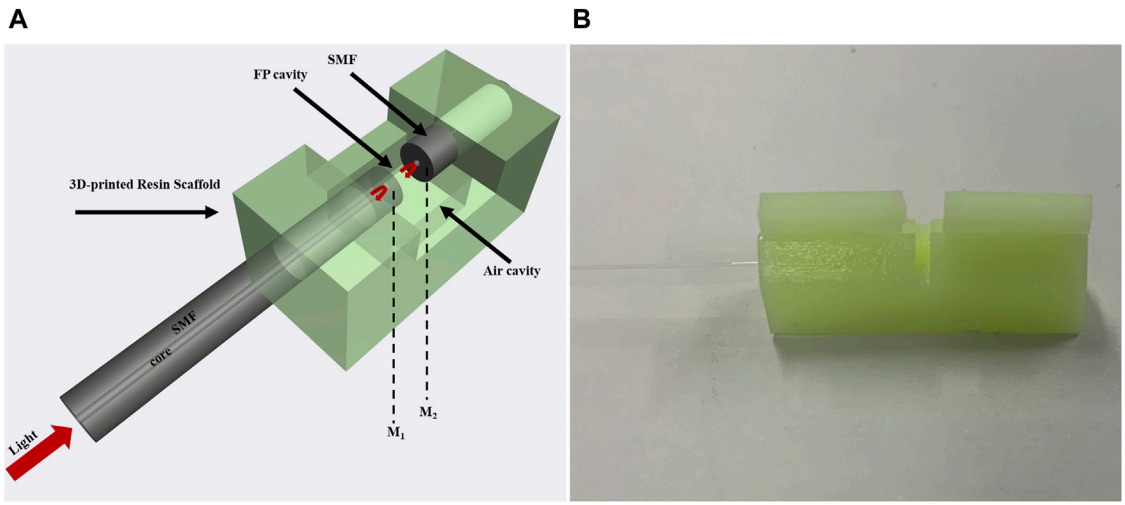

FIGURE 2
(A) Schematic diagram of FPI structure. **(B)** Physical diagram of FPI structure.

cost-effectiveness render it a quintessential component within CPSS infrastructures. The sensor also provides significant insights that advance sensor technology and environmental monitoring research.

2 Structure fabrication and sensing principle

The fabrication process of the FPI structure can be divided into three steps: firstly, a scaffold for embedding optical fibers is 3D printed with resin materials as shown in Figure 1A. Then an optical fiber with a smooth end face is embedded at one end of the resin scaffold and fixed with UV glue, as shown in Figure 1 b). Finally, an optical fiber with a smooth end face is embedded in the same way on the other side of the resin scaffold, so that a Fabry-Perot interferometer is constructed as shown in Figure 1C.

The 3D structure is shown in Figure 2A: two light-reflecting surfaces are constructed on the left and right optical fiber end faces (M_1 and M_2) to form a Fabry-Perot interferometer. The light entering the fiber from the left side propagates in the SMF, partially reflects through M_1, and the remaining light is transmitted in the air cavity and then reflected again in M_2. Eventually, these reflected beams form an interference in the left SMF. The wavelength of the inclination of the reflection spectrum can be defined as:

$$\lambda_m = \frac{4nL}{2m+1}, \tag{1}$$

where m is the order of the interference fringes (m is an integer), n is the effective refractive index of air and L is the F-P air cavity length. The distance between λ_m and λ_{m+1} is called free spectral range (FSR) and can be expressed as:

$$FSR = \frac{\lambda_m^2}{2nL}, \tag{2}$$

as can be seen from Eq. 2, when the refractive index is constant, a change in the length of the cavity will inevitably lead to a change in its FSR. The optical fiber coupling platform is used to control the horizontal movement of the optical fiber to change the cavity length, and the microscope photograph and the corresponding reflectance spectrum are shown in Figure 3. It can be seen that increasing the length of the cavity will lead to a corresponding decrease in the FSR, which is consistent with Eq. 2.

For wavelength demodulation, a change in the total length of the FPI cavity results in a shift in the peak of the interference spectrum. By taking the derivative of Eq. 1, the temperature sensitivity can be expressed as:

$$S_T = \frac{\partial \lambda_m}{\partial T} = \lambda_m\left(\frac{1}{n}\frac{dn}{dT} + \frac{1}{L}\frac{dL}{dT}\right) = \lambda_m(\alpha + \xi), \tag{3}$$

where α refers to the TOC of the cavity medium (air), with a sensitivity less than -0.86×10^{-6}/°C. ξ refers to the temperature sensitivity of the FPI cavity, which can be expressed as:

$$\frac{TEC_m \times L_m - TEC_s \times L_s}{L}, \tag{4}$$

among them, TEC_m and TEC_s refer to the thermal expansion coefficient of resin material and silicon dioxide, respectively. L_m and L_s refer to the length of resin material and optical fiber, respectively. And L is the length of the FP cavity. The TEC of the resin material is about 1×10^{-4}/°C, and we can see that the TEC of the resin material is two orders of magnitude higher than the TEC of silicon dioxide (about $\times 0.510^{-6}$/°C), so the influence of fiber and air in the test can be ignored. Due to the large TEC of the resin material, L_m rapidly elongates or shortens under temperature changes, causing the corresponding elongation or shortening of L, which will cause a wavelength shift in the inclination angle of the interference light according to Eq. (1). For this purpose, we fabricated an FPI sensor with a L_m of about 1068 μm and an L of about 121 μm for testing (Figure 4).

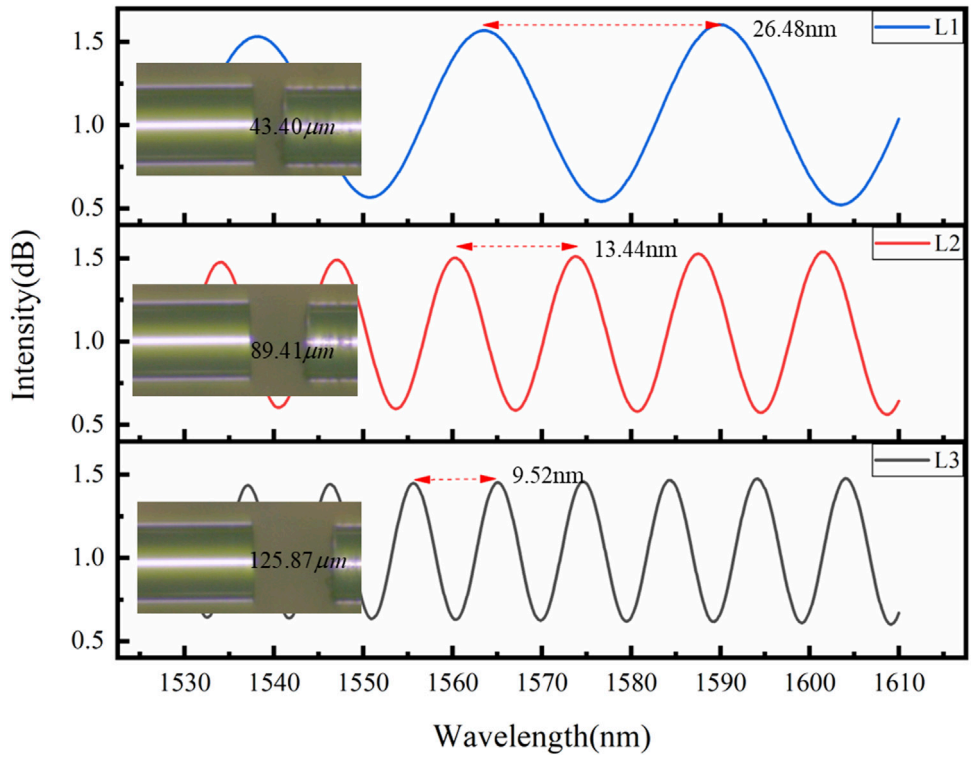

FIGURE 3
Microscope images and Reflectance spectra of sensor samples of different lengths.

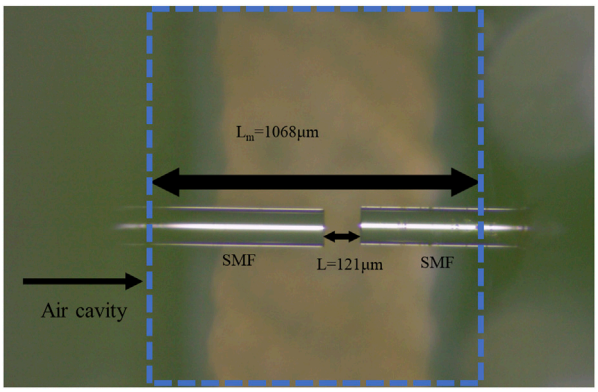

FIGURE 4
Microscope image of the FPI sensor.

3 Experiment and results discussion

The experimental test schematic diagram is shown in Figure 5. The instruments in the system include a fiber optic circulator, a heating platform (0.1°C accuracy), a temperature sensor (0.1°C accuracy), a broadband light source ASE (wavelength range from 1530 nm to 1610 nm), and a spectrum analyzer (OSA, MS9740A with a resolution of 0.1 nm). A broadband light source is emitted from ASE, and the light is fed to the proposed FPI structure via a fiber optic circulator, and the reflected light is collected by a spectrum analyzer. The FPI structure is fixed on the heating platform, and the temperature is controlled by the heating platform. The FPI structure and the temperature sensor are covered with a plastic Petri dish to ensure the uniformity of the temperature in the space above the heating platform, and the real-time temperature in the Petri dish is monitored with a temperature sensor to correct the temperature error. In the experiment, the heating platform provided temperatures from 35 °C to 39 °C, and the actual recorded temperatures under the correction of the temperature sensor were 34.9°C, 35.8°C, 36.6°C, 37.5°C and 38.4 °C.

Figure 6 show the relationship between wavelength and temperature of the FPI structure, with the temperature increasing, the peak wavelength exhibits a redshift, with the temperature decreasing, the peak wavelength exhibits a blue shift. The trough around 1538 nm is selected for tracking, and its temperature sensitivity reaches 14.330 nm/°C and 13.772 nm/°C when the temperature increases and decreases, respectively.

Stability is an important indicator of the sensor, and to test the stability of this FPI structure, we set the temperature to 36.6 °C and recorded the reflectance spectrum every 10 minutes for 1 h. Select four different wavelengths (1543 nm, 1562 nm, 1581 nm, 1600 nm) to track and record its wavelength shift, as shown in Figure 7, the wavelength of each trough is slightly moved back and forth between long wavelength and short wavelength, and the maximum wavelength shift of different troughs were 1.76 nm, 1.84 nm, 1.76 nm and 1.76 nm, and the temperature offset corresponding to wavelength changes is 0.12°C, 0.13°C, 0.12°C and 0.12 °C. Considering the regularity of wavelength back-and-forth shifts,

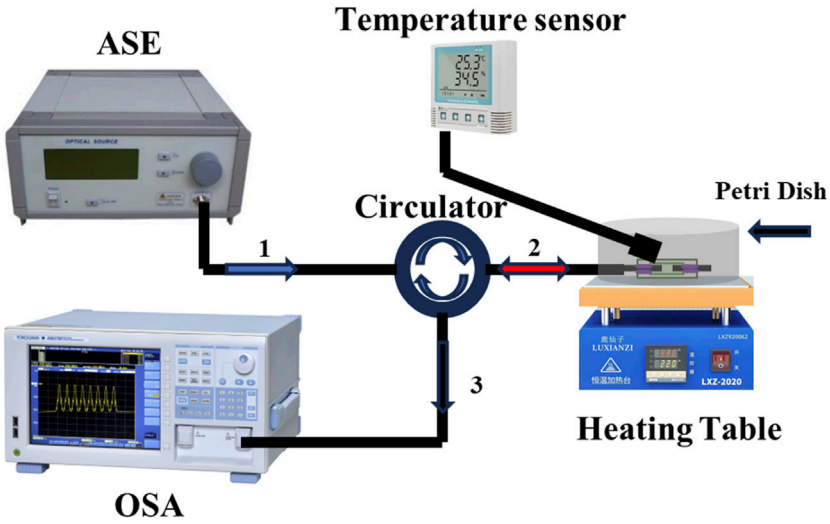

FIGURE 5
Experimental establishment of the temperature sensing system.

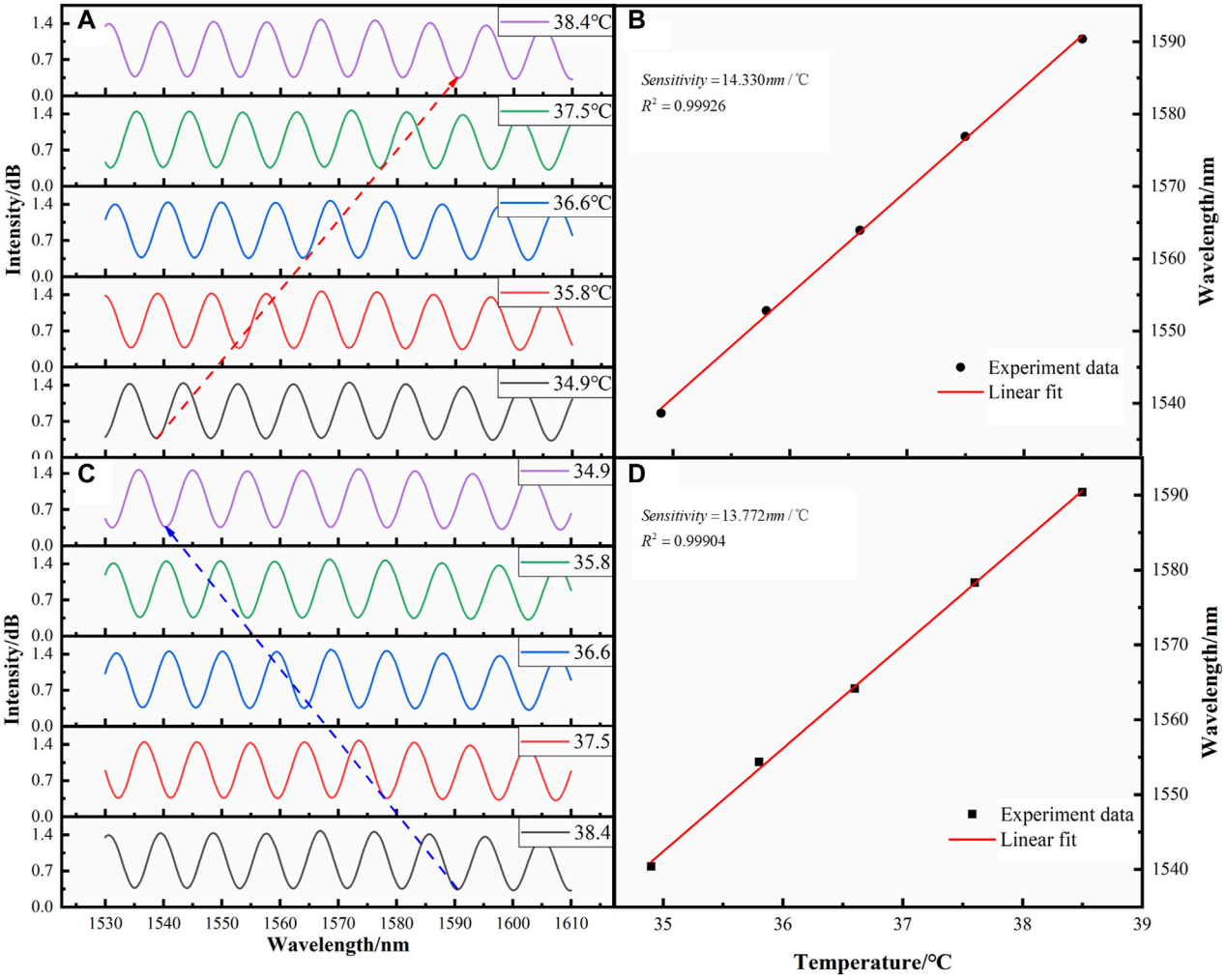

FIGURE 6
(A) The wavelength of the sensor is shifted to the right with increasing temperature. **(B)** Temperature sensitivity of wavelength demodulation. **(C)** The wavelength of the sensor is shifted to the left with decreasing temperature. **(D)** Temperature sensitivity of wavelength demodulation.

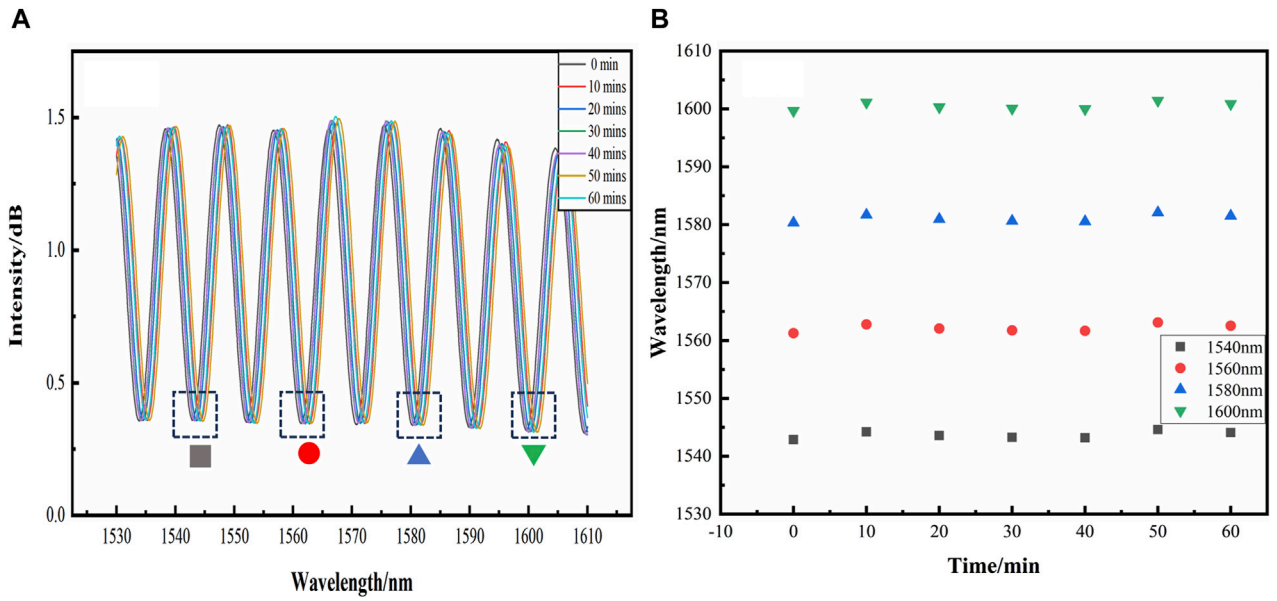

FIGURE 7
Test results of the stability of the sensor at 36.6°C. **(A)** Reflectance spectra recorded at 10-minute intervals. **(B)** Movement of the reflectance spectrum trough.

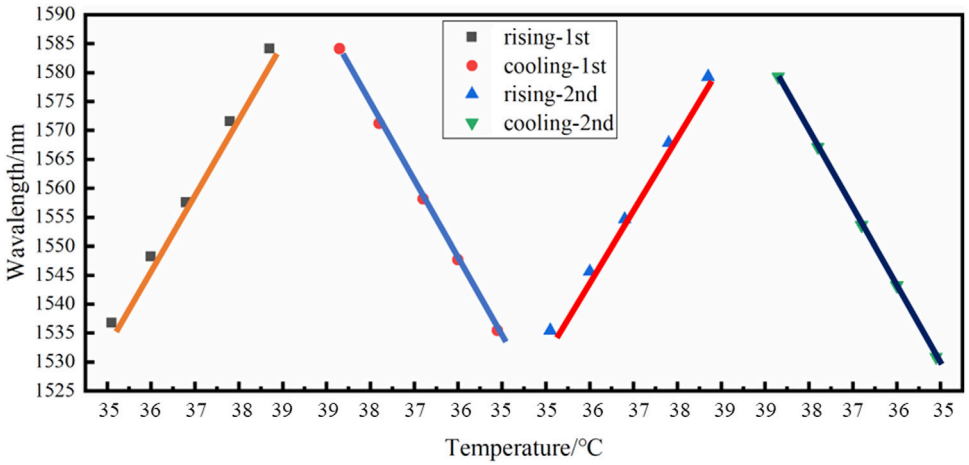

FIGURE 8
Repeatable experimental results of the sensor.

it can be speculated that this phenomenon may be caused by ambient temperature fluctuations.

Repeatability is also an important indicator of the sensor, and we have also performed repeatability experiments on this FPI structure. As shown in Figure 8, we first warmed the heating table from 35.1°C to 38.7°C, then cooled it down to 35.1°C, and then repeated once to get two cycles. From the figure, we can see that after a continuous heating and cooling cycle, the peak finally stays at a shorter wavelength, with a cycle lag of about 5.84 nm, the temperature sensitivity changes are about 0.889 nm/°C and 0.008 nm/°C, respectively.

The proposed temperature sensor is compared with the recently proposed temperature sensors as shown in Table 1. Compared with [17], the sensitivity of the temperature sensor we proposed is greatly improved. In [21], there are multiple reflective surfaces in the sensor, resulting in multiple light interference, which brings great difficulties to the demodulation. The sensing structure in [22] has a higher temperature sensitivity, but the liquid is not stable enough, and the cavity length is difficult to control. In our sensors, the reflective surface is a fiber end face, which is structurally stable, and the cavity length can be adjusted with a fiber coupling platform. In [23], filling the capillary with UV polymer greatly improves the strength and sensitivity of the sensor

TABLE 1 Sensing performance comparison of the proposed sensor with reported sensor.

Sensor structure	Range (°C)	Sensitivity	Ref.
UV polymer-capped	40~90	249 pm/°C	[17]
Capillary/PDMS	20~120	2.62 nm/°C	[21]
Liquid-Air Cavities	34.3~36.1	39.21 nm/°C	[22]
Capillary/UV polymer	39~54	1226.64 pm/°C	[23]
Resin-Fiber Structure	34.9–38.5	14.330 nm/°C	This Work

while controlling the cavity length, but the sensitivity is limited due to the difficulty of making a longer cavity length.

Nevertheless, the proposed sensor still has some shortcomings, due to the F-P open cavity, the reflective surfaces are susceptible to dust contamination in the air. At the same time, compared with the traditional fiber optic sensor, the addition of the resin bracket greatly increases the volume of the sensor, but this problem can be improved by improving the structure of the resin stent.

4 Conclusion

In this study, we address the demand for high-precision environmental monitoring within CPSS by successfully developing and empirically validating a novel high-sensitivity temperature sensor. Uniquely designed to function efficiently within the CPSS framework, this sensor exhibits remarkable sensitivity, with a resolution of 14.330 nm/°C in the critical range of 35–39°C. It is constructed with two coaxial fibers embedded in a resin support, which is fabricated using advanced 3D printing technology, enabling ease of production and demodulation. Moreover, the sensor responds swiftly to real-time environmental changes, enhancing its applicability within CPSS.

Empirical tests have confirmed the sensor's attributes: heightened sensitivity, superb linearity, and steadfast stability within the temperature range of 34.9°C–38.4°C, thereby meeting and exceeding the stringent requirements for accuracy and reliability in CPSS applications.

The significance of this study transcends its technological innovation; it also makes a substantial contribution to the enhancement of smarter, more interconnected CPSS environments. The findings offer an efficacious technical solution for environmental monitoring that has potential implications for smart cities, intelligent transportation systems, and advanced building automation.

In summary, our research introduces an innovative approach to high-precision temperature monitoring and environmental sensing within CPSS, establishing a foundational platform for continued scientific inquiry and practical innovation in the domain. We anticipate that this technology will spur further advancements in CPSS research and contribute substantially to the development of an intelligence-driven, efficient, and secure societal infrastructure.

Data availability statement

The original contributions presented in the study are included in the article/Supplementary material, further inquiries can be directed to the corresponding author.

Author contributions

YZ: Conceptualization, Methodology, Project administration, Writing–original draft, Writing–review and editing. PZ: Conceptualization, Methodology. ZL: Formal Analysis, Investigation, Writing–review and editing. JS: Methodology, Supervision, Writing–review and editing. CL: Project administration, Resources, Writing–review and editing.

Funding

The author(s) declare financial support was received for the research, authorship, and/or publication of this article. This work was supported by the Finance Science and Technology Project of Hainan Province (ZDKJ2020009).

Conflict of interest

The authors declare that the research was conducted in the absence of any commercial or financial relationships that could be construed as a potential conflict of interest.

Publisher's note

References

1. Gao H, Jiang Y, Zhang L, Cui Y, Jiang J, Jiang L, et al. Antiresonant mechanism based self-temperature-calibrated fiber optic Fabry–Perot gas pressure sensors. *Opt Express* (2019) 27:22181–9. doi:10.1364/oe.27.022181

2. Li Z, Zhang Y-X, Zhang W-G, Kong L-X, Yan T-Y, Geng P-C, et al. High-sensitivity gas pressure fabry–perot fiber probe with micro-channel based on vernier effect. *J Light Technol* (2019) 37:3444–51. doi:10.1109/jlt.2019.2917062

3. Xu F, Ren D, Shi X, Li C, Lu W, Lu L, et al. High-sensitivity Fabry–Perot interferometric pressure sensor based on a nanothick silver diaphragm. *Opt Lett* (2012) 37:133–5. doi:10.1364/ol.37.000133

4. Quan M, Tian J, Yao Y. Ultra-high sensitivity Fabry-Perot interferometer gas refractive index fiber sensor based on photonic crystal fiber and Vernier effect. *Opt Lett* (2015) 40:4891–4. doi:10.1364/ol.40.004891

5. Ffu HY, Tam HY, Shao L, Dong X, Wai A, Lu C, et al. Pressure sensor realized with polarization-maintaining photonic crystal fiber-based Sagnac interferometer. *Appl Opt* (2008) 47:2835–9. doi:10.1364/ao.47.002835

6. Martynkien T, Statkiewicz-Barabach G, Olszewski J, Wojcik J, Mergo P, Geernaert T, et al. Highly birefringent microstructured fibers with enhanced sensitivity to hydrostatic pressure. *Opt Express* (2010) 18:15113–21. doi:10.1364/oe.18.015113

7. Lin C, Qiu C, Jiang H, Zou L. A deep neural network based on prior-driven and structural preserving for SAR image despeckling. *IEEE J Selected Top Appl Earth Observations Remote Sensing* (2023) 16:6372–92. doi:10.1109/jstars.2023.3292325

8. Roriz P, Silva S, Frazao O, Novais S. Optical fiber temperature sensors and their biomedical applications. *Sensors* (2020) 20(7):2113. doi:10.3390/s20072113

9. Vargas-Rodriguez E, Guzman-Chavez AD, Baeza-Serrato R, Garcia-Ramirez MA. Optical fiber FP sensor for simultaneous measurement of refractive index and temperature based on the empirical mode decomposition algorithm. *Sensors* (2020) 20(3):664. doi:10.3390/s20030664

10. Li M, Liu Y, Gao R, Li Y, Zhao X, Qu S. Ultracompact fiber sensor tip based on liquid polymer-filled Fabry-Perot cavity with high-temperature sensitivity. *Sensors Actuators B: Chem* (2016) 233:496–501. doi:10.1016/j.snb.2016.04.121

11. Kong LX, Zhang YX, Zhang WG, Zhang YS, Yu L, Wang S, et al. High-sensitivity and fast-response fiber-optic micro-thermometer based on a plano-concave Fabry-Pérot cavity filled with PDMS. *Sensors Actuators A: Phys* (2018) 281:236–42. doi:10.1016/j.sna.2018.09.004

12. Liu Z, Xiao H, Liao M, Han X, Chen W, Zhao T, et al. PDMS-assisted microfiber MZ interferometer with a knot resonator for temperature sensing. *IEEE Photon Technol. Lett.* (2019) 31(5):337–40. doi:10.1109/lpt.2019.2892781

13. Mizuno Y, Theodosiou A, Kalli K, Liehr S, Lee H, Nakamura K. Distributed polymer optical fiber sensors: a review and outlook. *Photon Res* (2021) 9(9):1719–33. doi:10.1364/prj.435143

14. Xiong Y, Xu F. Multifunctional integration on optical fiber tips: challenges and opportunities. *Adv Photon* (2020) 2(06):64001. doi:10.1117/1.ap.2.6.064001

15. Liu Y, Yang D, Wang Y, Zhang T, Shao M, Yu D, et al. Fabrication of dual-parameter fiber-optic sensor by cascading FBG with FPI for simultaneous measurement of temperature and gas pressure. *Opt Commun* (2019) 443:166–71. doi:10.1016/j.optcom.2019.03.034

16. Urrutia A, Goicoechea J, Ricchiuti AL, Barrera D, Sales S, Arregui FJ. Simultaneous measurement of humidity and temperature based on a partially coated optical fiber long-period grating. *Sensors Actuators B: Chem* (2016) 227:135–41. doi:10.1016/j.snb.2015.12.031

17. Uyor UO, Popoola API, Popoola OM, Aigbodion VS. Polymeric cladding materials under high temperature from optical fibre perspective: a review. *Polym Bull* (2020) 77(4):2155–77. doi:10.1007/s00289-019-02830-y

18. Sun B, Wang Y, Qu J, Liao C, Yin G, He J, et al. Simultaneous measurement of pressure and temperature by employing Fabry-Perot interferometer based on pendant polymer droplet. *Opt Express* (2015) 23(3):1906–11. doi:10.1364/oe.23.001906

19. Cao K, Liu Y, Qu S. Compact fiber biocompatible temperature sensor based on a hermetically-sealed liquid-filling structure. *Opt Express* (2017) 25(24):29597–604. doi:10.1364/oe.25.029597

20. Wang C, Zhou B, Jiang H, He S. Agarose filled Fabry–Perot cavity for temperature self-calibration humidity sensing. *IEEE Photon Technol. Lett.* (2016) 28(19):2027–30. doi:10.1109/lpt.2016.2581990

21. Chen M, Zhao Y, Xia F, Peng Y, Tong R. High sensitivity temperature sensor based on fiber air-microbubble Fabry-Perot interferometer with PDMS-filled hollow-core fiber. *Sensors Actuators A: Phys* (2018) 275:60–6. doi:10.1016/j.sna.2018.03.044

22. Fu D, Liu X, Shang J, Sun W, Liu Y. A simple, highly sensitive fiber sensor for simultaneous measurement of pressure and temperature. *IEEE Photon Technol. Lett.* (2020) 32(13):747–50. doi:10.1109/lpt.2020.2993836

23. Lang C, Liu Y, Liao Y, Li J, Qu S. Ultra-sensitive fiber-optic temperature sensor consisting of cascaded liquid-air cavities based on Vernier effect. *IEEE Sens J* (2020) 20(10):5286–91. doi:10.1109/jsen.2020.2970431

24. Gao H, Xu D, Ye Y, Zhang Y, Shen J, Li C. Fiber-tip polymer filled probe for high-sensitivity temperature sensing and polymer refractometers. *Opt Express* (2022) 30(5):8104–14. doi:10.1364/oe.449852

25. Salunkhe TT, Choi HW, Park SJ, Kim JH, Kim IT. High sensitivity temperature sensor based on Fresnel reflection with thermosensitive polymer: control of morphology and coating thickness. *Jpn J Appl Phys* (2020) 59(SG):SGGG06. doi:10.7567/1347-4065/ab5c7d

26. Dominguez-Flores CE, Monzon-Hernandez D, Moreno-Basulto JI, Rodriguez-Quiroz O, Minkovich VP, Lopez-Cortes D, et al. Real-time temperature sensor based on in-fiber fabry-perot interferometer embedded in a resin. *J Lightwave Technol* (2019) 37(4):1084–90. doi:10.1109/jlt.2018.2886134

27. Liu S, Ji Y, Yang J, Sun W, Li H. Nafion film temperature/humidity sensing based on optical fiber Fabry-Perot interference. *Sensors Actuators A: Phys* (2018) 269:313–21. doi:10.1016/j.sna.2017.11.034